Journal of Computational Science 96 (2026) 102847

Contents lists available at ScienceDirect

Journal of Computational Science

journal homepage: www.elsevier.com/locate/jocs

Shape grammar for modeling Earth's bathymetry and performing tsunami simulations[☆]

Paweł Maczuga [a], Marcin Łoś [a], Albert Oliver-Serra [b], Eirik Valseth [c,d], Anna Paszyńska [e], Maciej Paszyński [a,*]

[a] AGH University of Krakow, Krakow, Poland
[b] University of Las Palmas de Gran Canaria, Las Palmas de Gran Canaria, Spain
[c] Norwegian University of Life Sciences, Ås, Norway
[d] Simula Research Laboratory, Oslo, Norway
[e] Jagiellonian University, Krakow, Poland

ARTICLE INFO

Keywords:
Shape grammar
Triangular mesh generation
Earth bathymetry
Tsunami simulations
Shallow water equations
Generalized α-scheme

ABSTRACT

We present a shape grammar for generating Earth's bathymetry. The shape grammar uses just two productions to define the Kossaczky mesh-refinement algorithm. The algorithm is then recursively applied to the sphere, starting with a partition into eight elements. As a refinement criterion, we select elements where Earth's bathymetry needs improvement, based on the Global Multi-Resolution Topography Data Synthesis. Given a computational mesh approximating Earth's bathymetry, we adopt the long-wave approximation derived from the shallow-water equations under appropriate assumptions to obtain the nonlinear wave equation. The wave equation is subsequently approximated by finite elements in space, and in time, we employ the generalized-α scheme. We present three numerical simulations. The first is the tsunami caused by an asteroid impact in the central North Atlantic Ocean. The second is the tsunami caused by the collapse of a volcano on the Canary Islands. The third is the simulation of the tsunami caused by the earthquake in the Valparaiso region of Chile. We also perform a verification of our shape grammar tsunami simulator.

1. Introduction

Tsunamis are highly energetic ocean waves caused by the sudden displacement of large masses of ocean water, originating most frequently from high-magnitude earthquakes or, less frequently, from underwater volcanic eruptions, the calving of glaciers, massive landslides, or meteorite impacts. Despite their high energy and speeds of up to several hundred kilometers per hour, tsunami waves may go unnoticed in the open ocean due to their low wave height (up to several dozen centimeters) and long length (up to several hundred kilometers). The situation changes, however, dramatically when tsunami waves reach the coastal zone, where they grow (often rapidly), reach heights of up to several dozen meters, break onto the land, and lead to extensive flooding.

This paper is the third paper in our series of research articles devoted to the development of a finite-element-method tsunami simulation employing graph-grammar models. In the first paper [1], we proposed a graph-grammar model of computational mesh generation that expresses the Rivara algorithm for arbitrary triangular meshes. The graph-grammar model that expresses the Rivara algorithm generates several additional unwanted mesh refinements due to the execution of the longest-edge refinement algorithm. We also employed a simple first-order stabilization method to simulate the asteroid tsunami phenomenon. This graph-grammar model has been improved into a composition graph-grammar model in [2], which still employs the Rivara algorithm and generates unwanted refinements, but the computational cost of the execution of the graph transformation was cheaper due to single one node representation of the triangular elements. We employed the composition graph-grammar model to simulate the break of the Northern European Enclosure Dam (NEED) and the flooding of the European coast.

The goal of this paper is to develop a shape grammar for stable computer simulations of tsunami propagation. For this purpose, we combine the following methods:

- The shape grammar method for generating a computational mesh covering the topography and bathymetry of the entire Earth

---

[☆] This article is part of a Special issue entitled: 'AI, HPC &Simulations' published in Journal of Computational Science.

[*] Corresponding author.
E-mail address: paszynsk@agh.edu.pl (M. Paszyński).

https://doi.org/10.1016/j.jocs.2026.102847
Received 5 January 2026; Received in revised form 26 February 2026; Accepted 17 March 2026

aims to enable accurate simulations of tsunamis and the effects of rising sea and ocean levels. This method allows for an adaptive reduction of the error resulting from approximating the problem geometry. In our case, the problem geometry consists of the seabed topography and the seashore, which are approximated using triangular finite elements generated by shape grammar algorithms. The adaptive algorithm generates a high-fidelity computational mesh, resulting in a low discretization error for a Partial differential Equation (PDE). The shape grammar uses two productions to express the Kossaczky mesh-refinement algorithm [3]. The refinements are based on data from the Global Multi-Resolution Topography Data Synthesis dataset [4].

- Higher-order and accurate time integration schemes, such as the generalized α-method, are used for stabilized simulations of the tsunami. This method reduces the error resulting from time discretization. The generalized α-method is of second order with respect to the time step.

There are the following novelties and benefits of using the shape grammar model proposed in this paper. It is the first shape grammar to directly model the Kossaczky mesh-refinement algorithm [3]. In other words, it is the shape grammar description of the Kossaczky mesh-refinement algorithm, which follows recursive partitions of the triangular elements. The presented shape grammar consists of two productions. The implementation of this shape grammar consists of traversing the edges of the triangular elements and checking whether each edge is surrounded by the two markers. If this is the case, we check whether this edge requires further refinements. If this is the case, then we execute the first rule that propagates the markers. If, on the other hand, the broken edge meets the accuracy criterion, we apply the second rule to close the local refinements. This model inherits all the benefits of the Kossaczky method, including only local refinements, and does not need to propagate unwanted refinements. In other words, this shape grammar prevents propagation of unwanted refinements and keeps the mesh refined only in local areas of interest.

We focus on the generation and adaptation of triangular computational meshes. Mesh refinement involves subdividing the elements of a mesh to create a finer, more detailed discretization. During this process, the original nodes of the mesh are retained, and the overall mesh topology remains unchanged. Typically, refinement is applied to elements with high numerical error to improve the solution's accuracy. An adaptive algorithm identifies which elements should be refined and applies certain mesh regularity conditions to maintain the quality of the refined elements.

We propose, for the first time, the application of shape grammar to adapt finite element meshes. Shape grammar is a rewriting system that processes shapes according to a set of rules. George Stiny and James Gips [5] introduced it as a tool for the automatic generation of paintings and sculptures. The shape grammars formally consist of terminals that are not replaced during the derivation process; markers, which are processed and replaced during the generation; the set of rules that replace markers and add some new terminals; and the initial state, which is an initial set of terminals and markers. Previously, graph grammars have been successfully used to model mesh refinements on both triangular and rectangular elements [6–9]. The mesh refinement algorithms employed in these works use the concept of hanging nodes and the 1-irregularity rule, which makes the implementation very complex. The implementation of the hanging node requires the so-called constraint approximation [10,11], where one edge is adjacent to one large element from one side in two dimensions and to two smaller elements on the other side. The functions used to approximate the solution on the small elements have to match the approximation of one large function on the big element side. Additionally, the 1-regularity rule requires several refinements to prevent multiple constrained nodes, which would necessitate even more complex constrained approximation rules.

Mesh refinements without hanging nodes are often processed by the Rivara longest-edge refinement algorithm [12,13]. The Rivara algorithm has already been defined using another kind of transformational rules, called the hypergraph grammar, in [14]. The previous model described in [14] employed the hypergraph grammar approach. It requires six hypergraph grammar productions, as illustrated in Figures 5–10 of [14]. An alternative model using the composition of graph-grammar productions [2] operates with four graph-grammar productions, see Figures 4, 5, 6, and 8 in [2]. Our new shape grammar model uses just two rules for shape grammar refinement (actually, it is just one rule with or without the terminal mark).

2. Shape grammar for modeling Earth's bathymetry

The shape grammar is given by:

$SGI = \langle V_T, V_M, R, I \rangle,$ (1)

where:

$V_T = \{$ 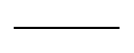 $\},$ (2)

V_T stands for the set of terminals; in our case, they denote the edges of the triangles of the mesh.

$V_M = \{$  $\},$ (3)

V_M stands for the set of markers.

$R = \{$ $rule_1 =$ 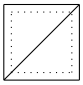 $\rightarrow$ 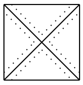 $, rule_2 =$ 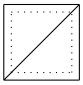 $\rightarrow$ 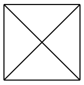 $\},$ (4)

R is the set of rules, and, in general, I denotes the initial state.

As an example, consider the initial state:

$I =$ 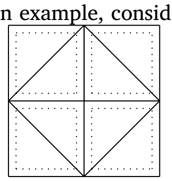

we have the following possible derivation:

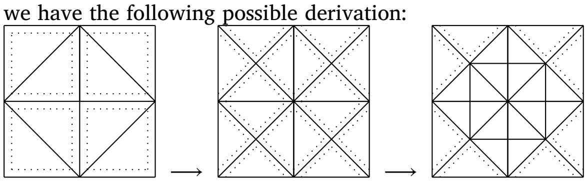

In our case, for the purpose of generating a mesh from Earth's topography, we replace the initial symbol with a sphere partitioned into 8 triangles:

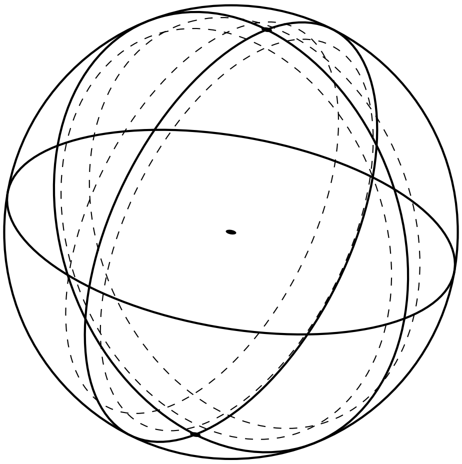

$I =$

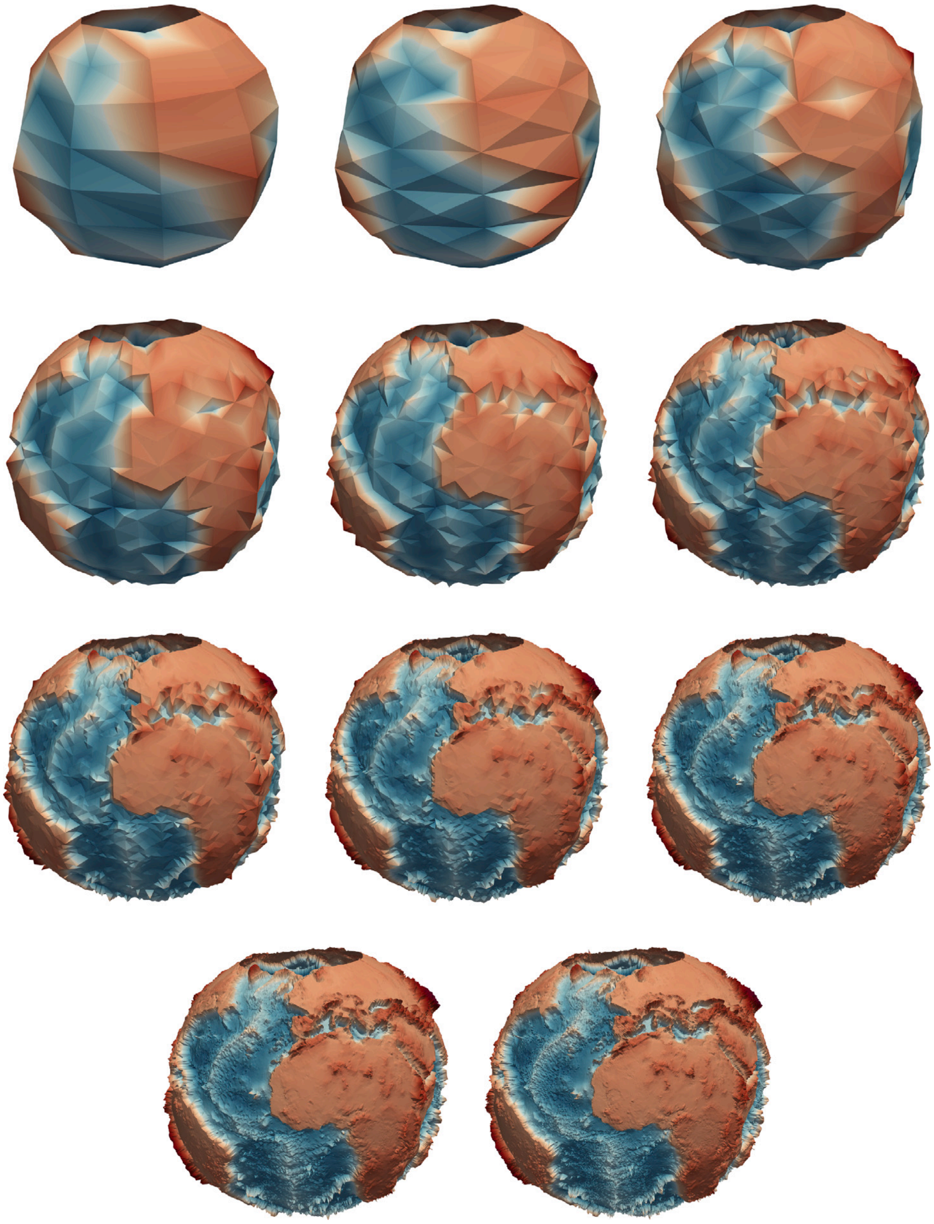

Fig. 1. Eleven snapshots from the generation of the computational mesh approximating the topography and bathymetry of the whole Earth, by using the Kossaczky method modeled by shape grammar, generated over the sphere domain.

I represents an initial state. Our initial state is a sphere partitioned into 8 triangular elements, with each element containing a marker. The marker line follows the azimuthal circles but does not follow the equator. The shape grammar has been employed to generate the bathymetry of the Earth, including the seashore and the ocean floor. Our mesh refinements employ the Global Multi-Resolution Topography Data Synthesis dataset [4]. We identify all points on the map that lie within the triangle for which we have elevation data. For each point, we calculate the absolute value of the difference between the map elevation and the elevation estimated from the triangle. We mark this triangle for improvement if the absolute value for any point exceeds the set tolerance. The mesh generation and adaptation process is illustrated in Fig. 1. The final mesh is illustrated in Fig. 2.

3. Tsunami simulations over the Earth bathymetry

A fundamental component of our simulation framework is the numerical solution of wave equations that capture the dynamics of large-scale tsunami-like phenomena. A detailed overview of tsunami wave modeling can be found in [15]. Seawater motion is frequently approximated by the shallow water equations (SWE), which constitute a nonlinear system of transient partial differential equations [16]. Due to their nonlinearity and multiple unknowns, SWE solutions are computationally expensive. However, several simplified models exist that maintain good accuracy under specific assumptions. For tsunami scenarios, we use the nonlinear wave equation resulting from the long-wave approximation of the SWE under appropriate assumptions [1,17,18]:

$$\frac{\partial^2 u}{\partial t^2} - \nabla \cdot \left(g(u - h_b)\nabla u \right) = 0 \quad \text{in } \Omega, \tag{5}$$

where u denotes the water surface elevation, h_b represents the bathymetric depth , $g = 9.81$ m/s^2 the gravitational constant, and Ω the computational domain, i.e., the earth surface (see Fig. 3). A derivation of the non-linear wave equation from the Navier–Stokes equations is presented in [19]. Our equation corresponds to Eq. (6) [page 63] in [19] assuming $\nu = 0$ (kinematic viscosity) so the $\frac{\partial h}{\partial t}$ term disappears. There, $H = u - h_0$ and h_0 correspond to h_b in this paper. There are some

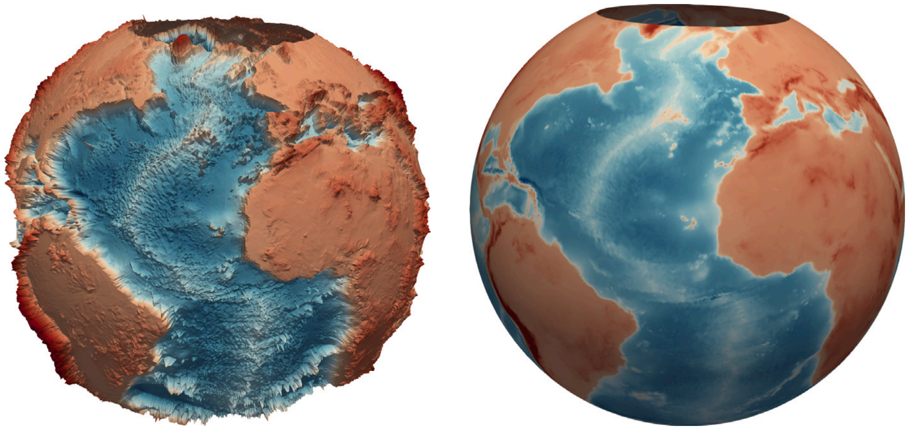

(a) Final mesh of the Earth. The Earth's radius is set to 60 000 meters (around 100 times smaller than real one) to better see the topography.

(b) Mesh of the Earth with real-life radius (6 378 000 m). Same initial mesh and same number of iterations as in the left picture.

Fig. 2. Final mesh of the Earth. Let panel presents the topography and bathymetry of the mesh scaled 100 times (100 times smaller radius of the sphere but the same variability of the heights like in the real model) for better presentation of the topographical variability. Right panel presents the real scale.

simplifying assumptions taken into account while deriving (6) [page 63] in [19]. Namely,

- The derivation starts from the Navier–Stokes equations that have been integrated from the seabed to the surface.
- The resulting equations are linearized about the still water base flow.
- In the derivation of the shallow water equations, we also assumed that the pressure in the flow is hydrostatic (proportional to the depth of the water).
- We also assume that the atmospheric pressure is constant (say zero) along the free surface.
- Finally, we assume that the vertical gradients of the velocity dominate, so we can estimate the vorticity at the seabed.
- Additionally, we assume that there are small angles of the seabed which corresponds with the approximation of $\frac{\partial h_0}{\partial x} = \frac{\partial h_0}{\partial y} = 0$ there (or $\frac{\partial h_b}{\partial x} = \frac{\partial h_b}{\partial y} = 0$ using the notation from this paper).
- We also assume zero kinematic viscosity for the seawater, so the $\frac{\partial h}{\partial t}$ term disappears. For the water, this coefficient is actually of the order of $10^{-6}[\mathrm{m}^2/\mathrm{s}]$ (very small), which justifies this assumption.

The equation assumes the wave speed is given by $c^2 = g(u - h_b)$, a standard result for shallow water waves. During our derivation, following [19], it is assumed that there are small angles of the seabed. This means that our model may not be very accurate near the seashore, particularly in areas with steep bathymetry (shallow water). However, it can still model the propagation of waves on large scales in the oceans.

The computational domain covers the entire Earth, with Neumann boundary conditions implicitly enforced at the poles. We use a shape grammar-based mesh generation approach to construct a global finite element mesh in spherical coordinates (λ, ψ). The reference water level aligns with a spherical Earth surface. The water level and bathymetry are described as scalar fields $u(\lambda, \psi)$ and $h_b(\lambda, \psi)$, respectively. Bathymetric and topographic data are sourced from the Global Multi-Resolution Topography dataset [4].

The mesh refinement from the initial state is driven by:

- **Height differences:** Triangles with a height error exceeding 100 m are refined.
- **Coastal features:** Triangles intersecting the sea level within a 100 m vertical range are also refined.

We use the following coordinate transformations from spherical to Cartesian:

$$
\begin{aligned}
x &= (\lambda - \lambda_0) R \cos \phi_0, \\
y &= R\phi,
\end{aligned} \tag{6}
$$

where (λ_0, ϕ_0) is a reference point and R is the Earth's radius. Applying the chain rule yields:

$$
\nabla \cdot \left(g(u - h_b)\nabla u\right) = \nabla \left\{ g(u - h_b) \frac{1}{R \cos \phi_0} \frac{\partial u}{\partial \lambda}, \quad g(u - h_b) \frac{1}{R} \frac{\partial u}{\partial \phi} \right\}^{\top}, \tag{7}
$$

which leads to the transformed wave equation in spherical coordinates:

$$
\frac{\partial^2 u}{\partial t^2} - R^2 \left(\frac{1}{\cos^2 \phi_0} \frac{\partial}{\partial \lambda} \left[g(u - h_b) \frac{\partial u}{\partial \lambda} \right] \right) - R^2 \frac{\partial}{\partial \phi} \left[g(u - h_b) \frac{\partial u}{\partial \phi} \right] = 0 \quad \text{in } \Omega. \tag{8}
$$

As tsunamis travel long distances across oceans, it is natural to include the effect of Coriolis forces, as Earth rotation can impact a tsunami [20]. With the wave equation in spherical coordinates, we add the Coriolis term:

$$
\frac{\partial^2 u}{\partial t^2} - R^2 \left(\frac{1}{\cos^2 \phi_0} \frac{\partial}{\partial \lambda} \left[g(u - h_b) \frac{\partial u}{\partial \lambda} \right] \right) - R^2 \frac{\partial}{\partial \phi} \left[g(u - h_b) \frac{\partial u}{\partial \phi} \right] + c_{CF} f^2 u = 0 \quad \text{in } \Omega, \tag{9}
$$

where the $f^2 u$ term represents the Coriolis force. Here $f = 2\omega sin(\phi)$ with ω the Earth angular velocity (which is 2Π in 24 h, which accounts for $\frac{2\Pi}{24 \times 3600} = 7.29 \cdot 10^{-5}$ [rad/s]), ϕ is the angular latitude, and c_{CF} is the scaling factor. The motivation for using this Cariolis force term is based on book [21]. In Section 7.2 (pages 191–193), there is a derivation[1] of the non-linear wave equation with Coriolis force in eq. (7.2.13). The Coriolis force there has a similar form to that in our paper. There, it is assumed that the Coriolis force term is $(-fv, fu)$, which corresponds to the rotational force in the spherical coordinates defined as $2\omega \sin(\theta)$ as in our paper. We subsequently discretize (9) in space using the finite element method and in time using the generalized-α scheme [22]. The weak form is given by:

$$
\left(\frac{\partial^2 u}{\partial t^2}, v \right) + b(u, v) = 0 \quad \forall v \in V, \tag{10}
$$

---

[1] referring to the paper of Thomas Kelvin “On gravitational oscillations of rotating water” 1879.

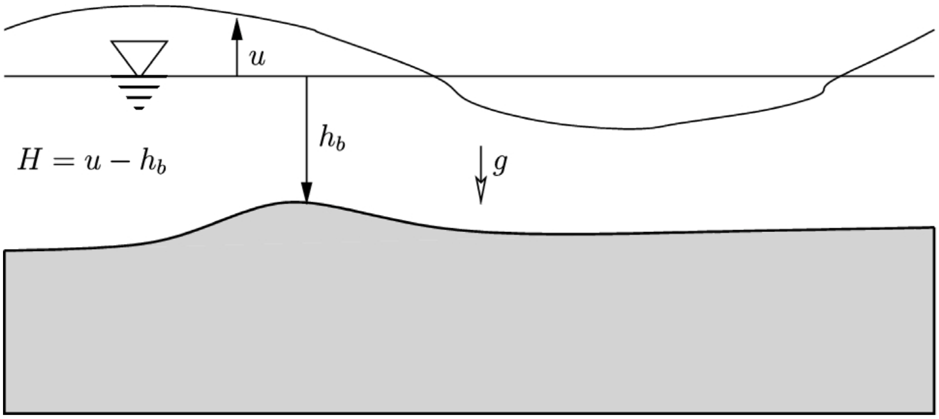

Fig. 3. Definition of water levels. Image from [2]. Here u represents the water level; h_b denotes the seabed; $H = u - h_b$ represents the water depth relative to the seabed. The acceleration due to gravity $g = 9.81[\frac{m}{s^2}]$.

with bilinear form $b(\cdot,\cdot)$:

$$b(u,v) = R^2 \; g\left((u-h_b)\frac{\partial u}{\partial \phi}, \frac{\partial v}{\partial \phi}\right) - \; R^2 \; g\frac{1}{\cos^2\phi_0}\left((u-h_b)\frac{\partial u}{\partial \lambda}, \frac{\partial v}{\partial \lambda}\right) + (c_{CF} f^2 u, v), \tag{11}$$

and V the test space. To mitigate numerical instabilities near shorelines, we add a damping term:

$$C_{\text{dump}} = C_0 \frac{h_0}{\min\{h_0, h_b\}}, \tag{12}$$

where $c_0 = 5 \times 10^{-4}$ and $h_0 = -5$ m. This damping is active only in shallow regions where $h_b \approx h_0$. Using the Bubnov–Galerkin method to discretize (10) in space, we arrive at the semi-discrete form:

$$M\ddot{\mathbf{u}} + C\dot{\mathbf{u}} + B\mathbf{u} = 0, \tag{13}$$

where M, C, and B are the mass, damping, and stiffness matrices, respectively. Defining $\mathbf{a} = \ddot{\mathbf{u}}$ and $\mathbf{v} = \dot{\mathbf{u}}$, the generalized-$\alpha$ scheme becomes:

$$M\mathbf{a} + C\mathbf{v} + B\mathbf{u} = 0, \tag{14}$$

with time-stepping update:

$$M\mathbf{a}_{n+1-\alpha_1} + C\mathbf{v}_{n+1-\alpha_2} + B\mathbf{u}_{n+1-\alpha_f} = 0, \tag{15}$$

and interpolated quantities:

$$\begin{aligned} \mathbf{a}_{n+1-\alpha_1} &= (1-\alpha_1)\mathbf{a}_{n+1} + \alpha_1 \; \mathbf{a}_n, \\ \mathbf{v}_{n+1-\alpha_2} &= (1-\alpha_2)\mathbf{v}_{n+1} + \alpha_2\mathbf{v}_n, \\ \mathbf{u}_{n+1-\alpha_f} &= (1-\alpha_f)\mathbf{u}_{n+1} + \alpha_f\mathbf{u}_n. \end{aligned} \tag{16}$$

Time integration is completed using:

$$\begin{aligned} \mathbf{v}_{n+1} &= \mathbf{v}_n + \tau\left[(1-\gamma)\mathbf{a}_n + \gamma\mathbf{a}_{n+1}\right], \\ \mathbf{u}_{n+1} &= \mathbf{u}_n + \tau\mathbf{v}_n + \frac{\tau^2}{2}\left[(1-2\beta)\mathbf{a}_n + \beta\mathbf{a}_{n+1}\right]. \end{aligned} \tag{17}$$

The method parameters depend on a spectral radius $\rho = 0.2$ and are computed as follows:

$$\begin{aligned} \alpha_1 &= \frac{2\rho-1}{\rho+1}, \quad \alpha_2 = \frac{\rho}{\rho+1}, \\ \beta &= \frac{1}{4}(1-\alpha_1-\alpha_2)^2, \quad \gamma = \frac{1}{2} - \alpha_1 - \alpha_2. \end{aligned} \tag{18}$$

This $\rho = 0.2$ parameter is responsible for damping of high frequencies, and all the values between (0,1) are appropriate, where 0 is a maximum damping, and 1 is a lack of damping. The selected value corresponds to significant damping of high frequencies, which is justified by the large scale of our tsunami simulations, and it improves the solver's stability. This parameter setup ensures that the time integration scheme is second-order [22].

4. Numerical results

4.1. Tsunami caused by asteroid at central North Atlantic Ocean

The sequence of images presented in Fig. 4 illustrates the evolution of a tsunami generated by an asteroid impact in the North Atlantic Ocean off the United States East Coast. The enormous kinetic energy from the asteroid impact forces the water column upward and outward, initiating the propagation of tsunami waves across the central North Atlantic Ocean.

From the simulation results, we can observe the developing wave spreading outward from the impact site as a concentric ring. A central depression, denoted in blue, follows the initial uplift, surrounded by an outward-propagating wave, denoted in red. These patterns reflect the circular nature of the tsunami waves, propagating symmetrically across the North Atlantic. However, the symmetry breaks as the waves interact with Ocean bathymetry and coastlines.

The tsunami waves interact with the coastline of the Caribbean and the eastern seashore of North America. The highest waves, denoted by red color, along the eastern United States, the Bahamas, and northern South America, reach twelve meters. The blue regions offshore mark the subsequent wave depression. At this stage, the tsunami exhibits complex interference and reflection patterns characteristic of large-scale ocean-basin wave dynamics. The amplification near the coasts implies that wave heights could rise dramatically, exceeding twelve meters, leading to severe destructive flooding once they reach land.

4.2. Canary Island volcano collapse tsunami

In this section, we describe a numerical simulation of a tsunami, presented in Figs. 5–6, generated by the collapse of a volcanic flank in the Canary Islands, representing the Cumbre Vieja Volcano on La Palma. The color scale indicates sea surface height (wave amplitude), with red showing elevated water levels and blue showing depressions. The initial water displacement caused by the volcanic flank collapse, where a large amount of geological material entering the ocean pushes water away, generates a wave that begins propagating outward into the North Atlantic Ocean. The wavefront expands further into the Atlantic, forming a circular propagation pattern. The energy disperses, and the amplitude decreases with distance from the source. Some energy begins to reach the coasts of northwest Africa and the Iberian Peninsula, while the main wave moves towards the open Atlantic. The tsunami waves have spread across the entire North Atlantic basin, with weaker but still visible disturbances reaching the Caribbean, South America, and the east coast of North America. Coastal regions on both sides of the Atlantic show localized intensification (red streaks), where the wave energy interacts with continental shelves. The wave pattern now

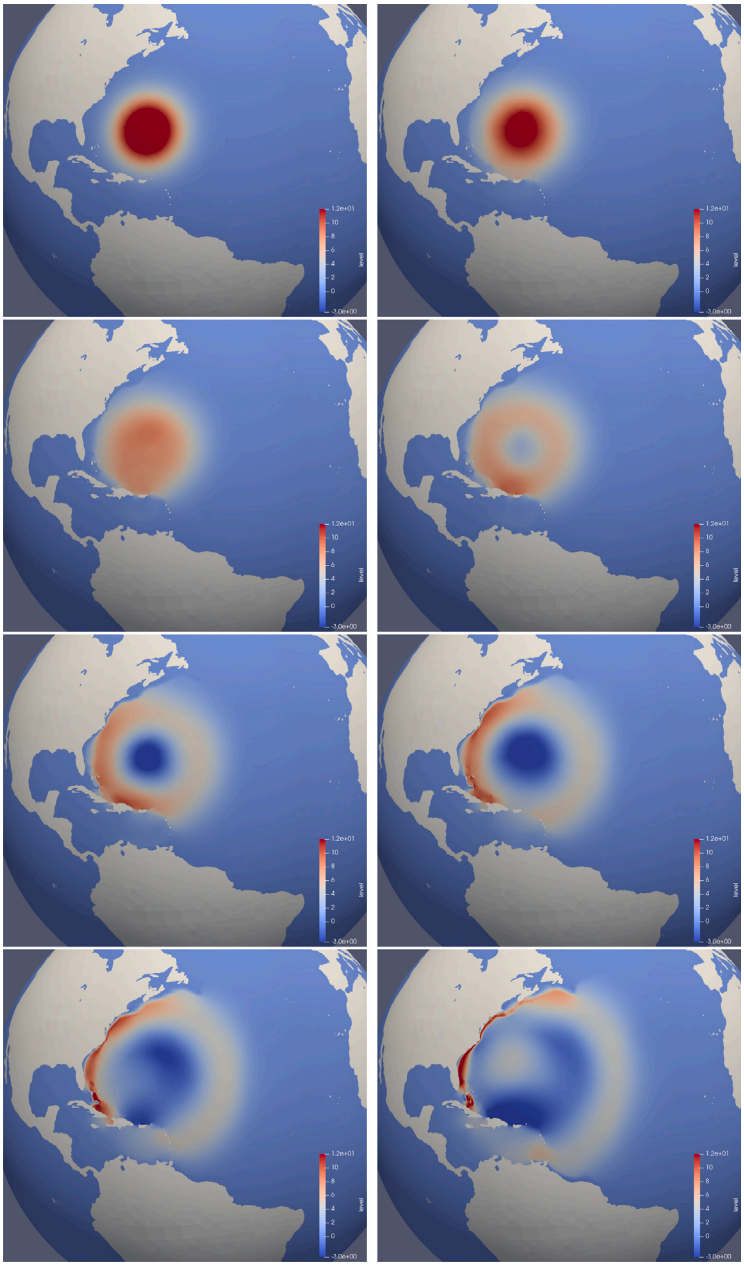

Fig. 4. Asteroid tsunami at the Atlantic ocean. Time moments t=20 m, t=30 m (first row) t=1h, t=1h 30 m (second row) t=2h, t=2h 30 m (third row), t=3h, t=3h 30 m (fourth row). The water level, varies from -3 m (dark blue) below the still water level to 12 m (red) above the still water level.

exhibits multiple reflections and interference, typical of basin-wide tsunami propagation after several hours.

4.3. Tsunami caused by the earthquake in the Valparaiso region of Chile

For the simulation of the earthquake-induced tsunami at the seashore of the Valparaíso region of Chile, we generated a high fidelity mesh in this area, as presented in Fig. 7. It provides a high resolution approximation of the seashore and the seabed Fig. 8. The tsunami caused by the earthquake, presented in Figs. 9–10, starts near the Valparaíso coastline — this represents the moment just after the Earthquake at the seabed, with maximum water elevation near the shore. The elevated water starts to move outward and downward, creating a circular wave traveling towards the seashore. Due to the large gradient of the seabed, this structure creates an elevated wavefront traveling towards the Valparaiso coastal region. The darker blue circle in the center denotes the depression created by the traveling wave. The wave moves towards the coastline, and it is elevated due to the structure of the seabed. Our model does not include interactions with the coastal region, so we stop the simulation the moment the front wave hits the coastal area. We can see from this figure that the predicted height of the wave is determined by the assumed height of the initial peak state.

5. Verification of the tsunami simulations

In this section, we present two verification methods for our tsunami simulations. First, we compare our simulation with the classic tsunami simulation repository, namely the catalog of Prof. Steven Ward, from the University of California, Santa Cruz (UCSC).[2] It contains a simulation of a massive tsunami caused by a volcanic landslide on the island

---

[2] https://ward.sites.ucsc.edu/

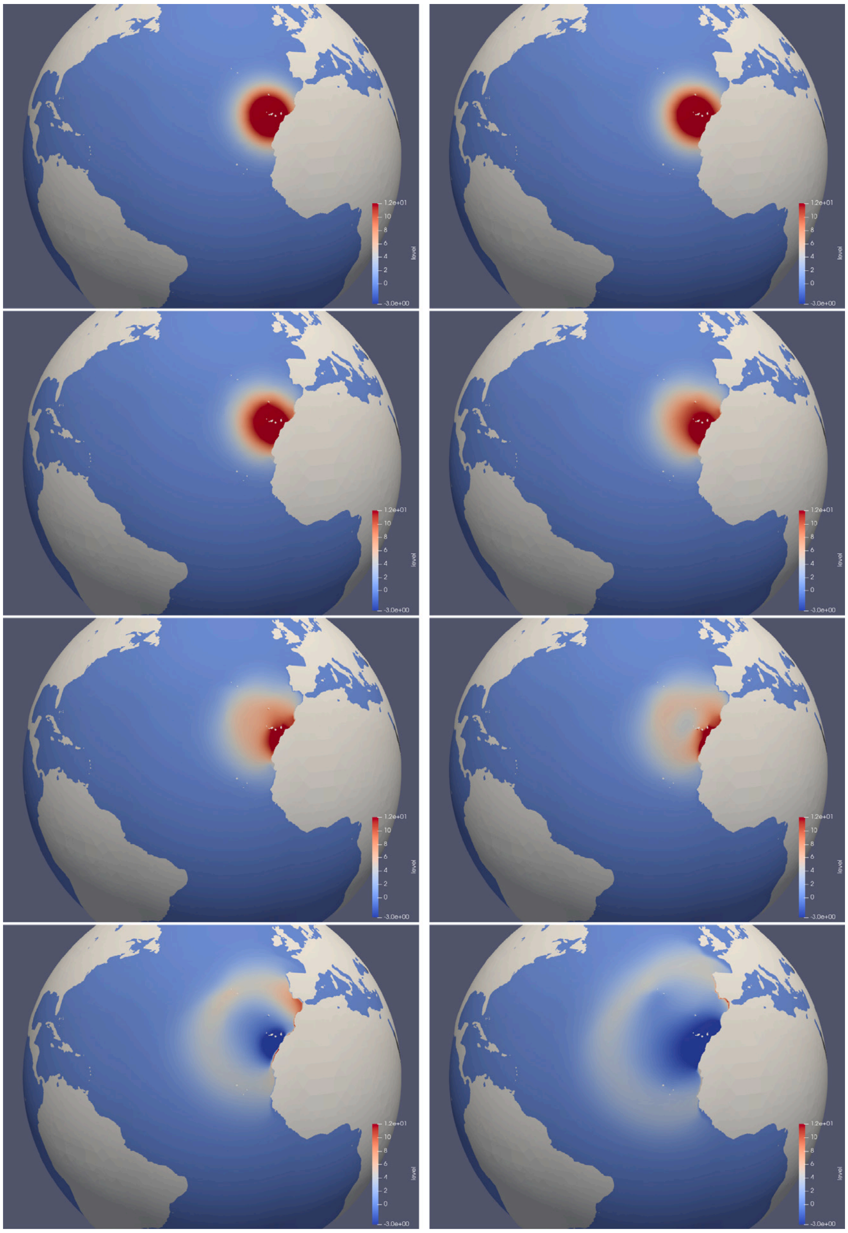

Fig. 5. Canary islands tsunami in the Atlantic ocean. Time moments t=20 m, t=30 m (first row) t=1h, t=1h 30 m (second row) t=2h, t=2h 30 m (third row), t=3h, t=3h 30 m (fourth row). The water level, varies from -3 m (dark blue) below the still water level to 12 m (red) above the still water level.

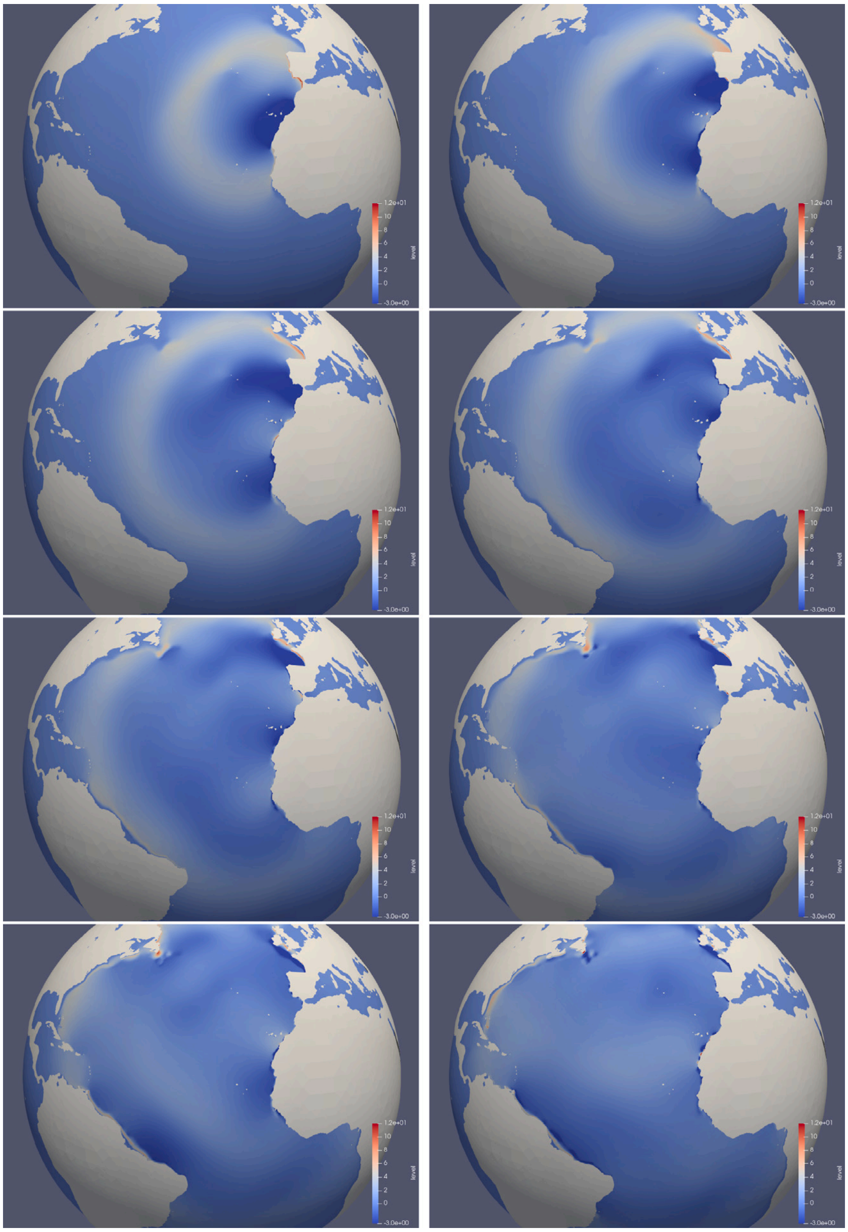

Fig. 6. Continuation of the Canary islands tsunami in the Atlantic ocean. Time moments t=4h, t=4.30 m (first row) t=5h, t=6h (second row) t=7h, t=8h (third row), t=9h, t=10h (fourth row). The water level, varies from -3 m (dark blue) below the still water level to 12 m (red) above the still water level.

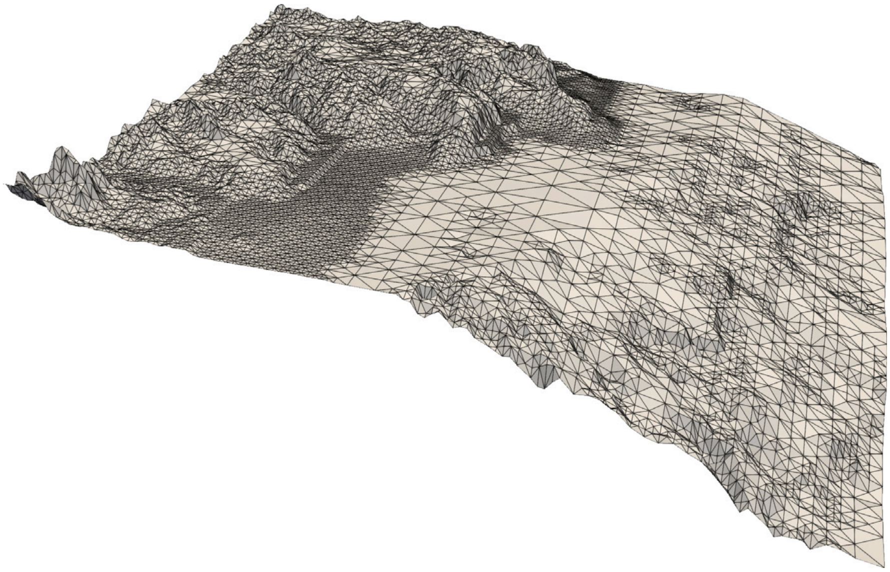

Fig. 7. Mesh approximating the bathymetry at the Valparaiso region of Chile. The area represents exact location of N-32.80, S-33.29 W-71.99 E-71.40. This part of the mesh has exactly 91,458 triangles and 45,957 vertices.

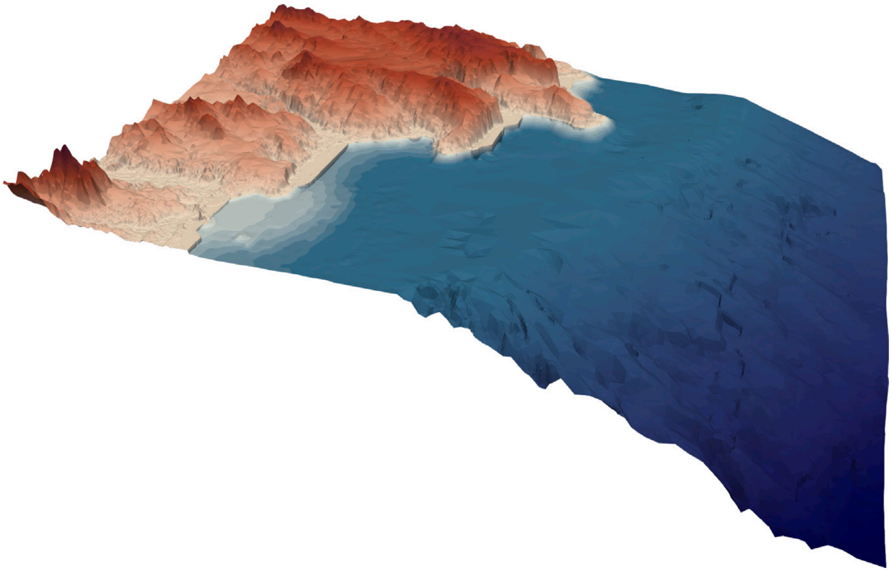

Fig. 8. Coastal area plotted based on the mesh approximating the bathymetry at the Valparaiso region of Chile. The area represents exact location of N-32.80, S-33.29 W-71.99 E-71.40.

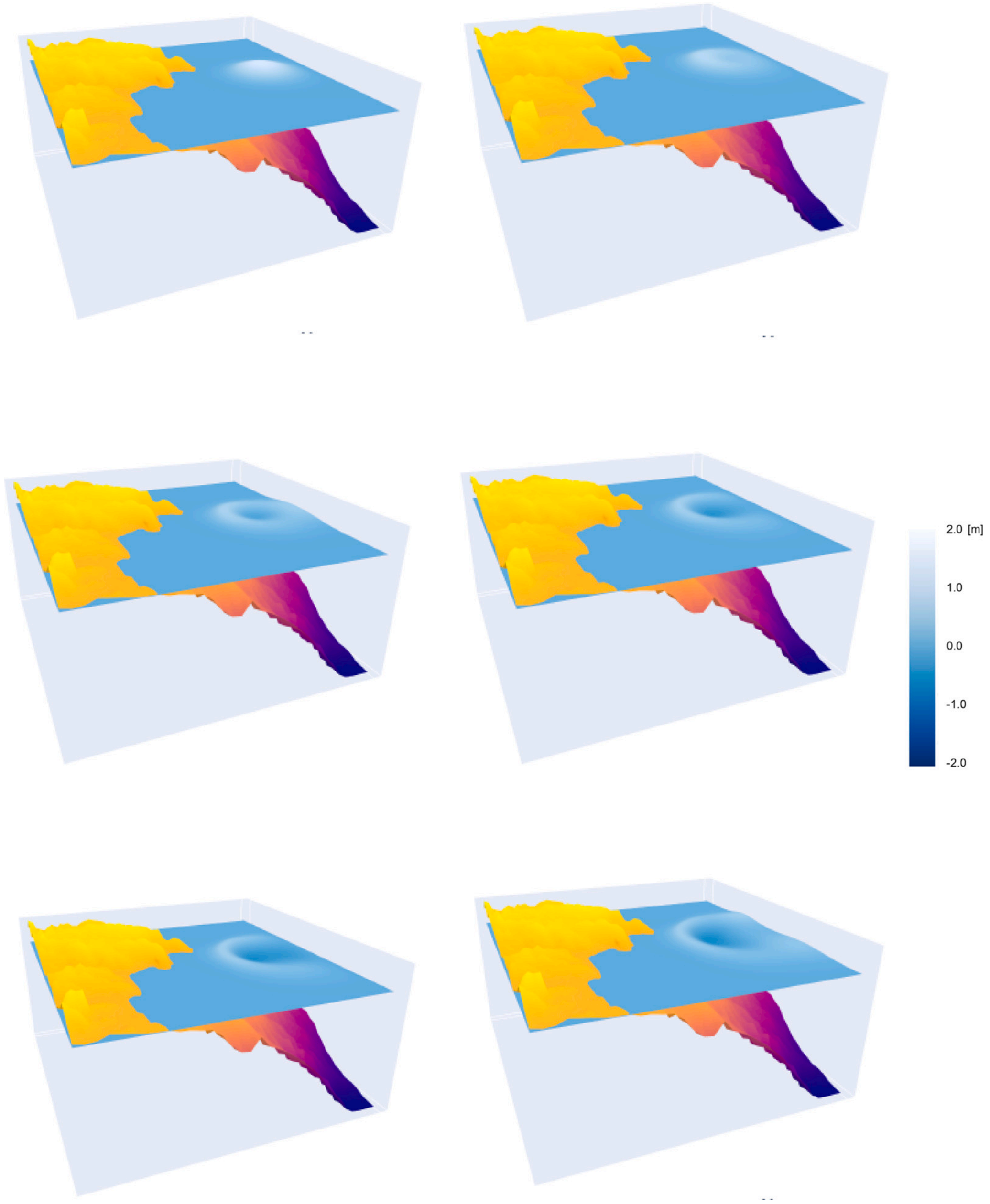

Fig. 9. Earthquake tsunami at the coast of Chile. Time intervals t=0s, t=12s (first row), t=24s, t=36s (second row), t=48s, t=1 m (third row). The water altitude is relative with respect to the.

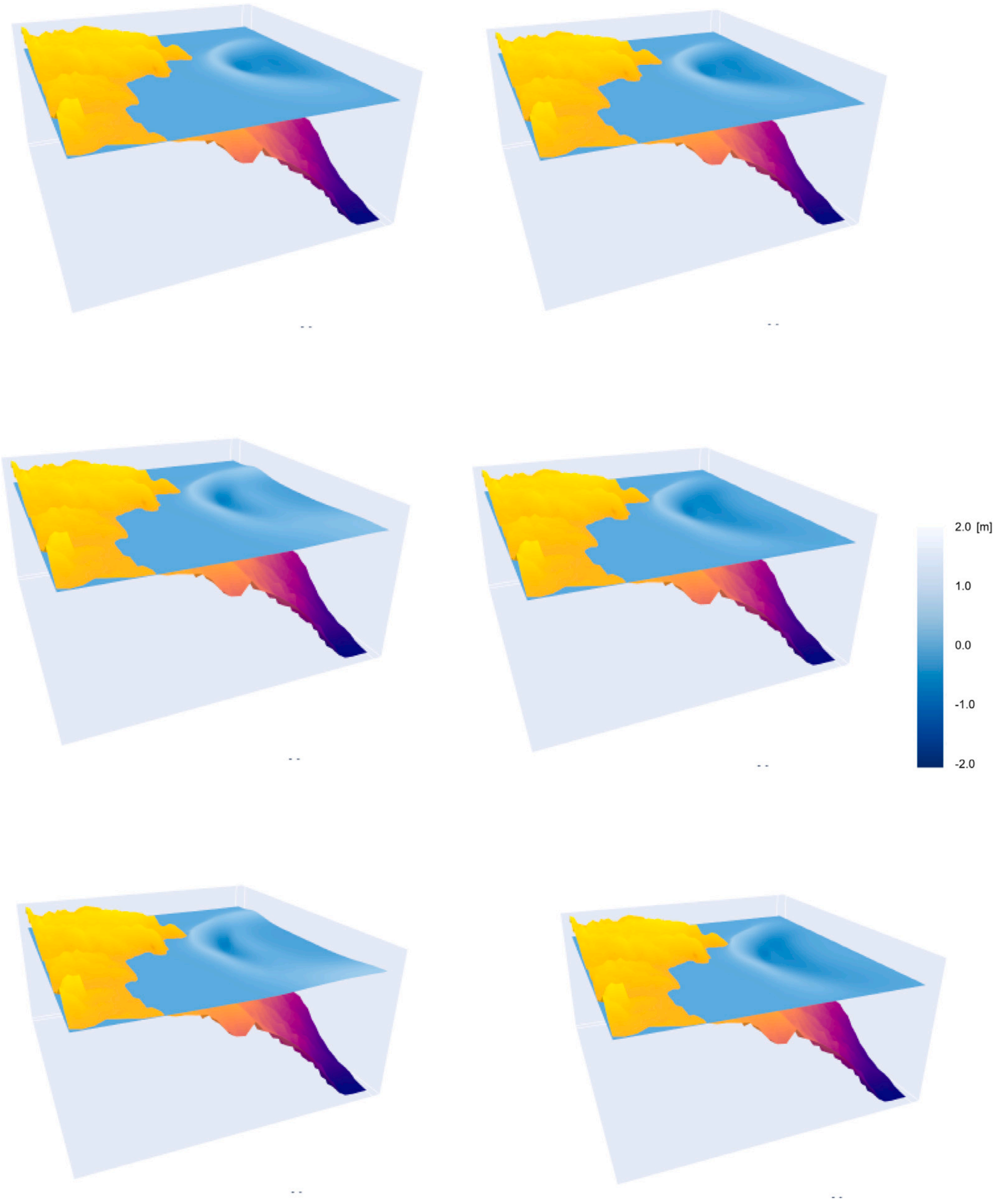

Fig. 10. Continuation of the earthquake tsunami at the coast of Chile. Time intervals t=1 m 12 s, t=1 m 24 s (first row), t=1 m 36 s, t=1 m 48 s (second row), t=2 m, t=2 m 12 s (third row).

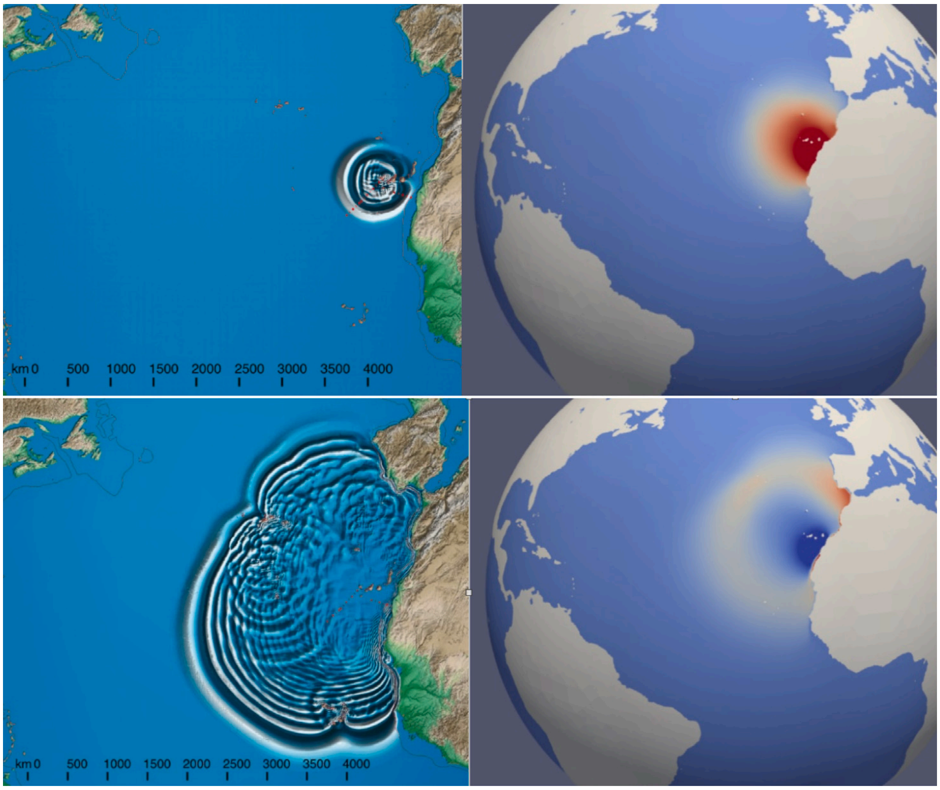

Fig. 11. Comparison of our tsunami simulations with a simulation of a massive tsunami caused by a volcanic landslide on the island of La Palma in the Canary Islands from Steven Ward repository https://ward.sites.ucsc.edu/LaPalma-TransAtlantic-nn/. Time moments t=1h 30 m (first row) t=3h (second row).

of La Palma in the Canary Islands. A comparison of the simulations, presented in Figs. 11–13 shows the similarity of the wave front.

A qualitative comparison of the wavefront gives satisfactory results; however, higher frequencies are attenuated in our simulation. The generalized alpha scheme we used in the simulation with coefficient $\rho = 0.2$ damps higher frequencies, which is justified by the large scale of our tsunami simulations, and it improves the solver's stability.

Second, we have added the "tsunami in the swimming pool" example to verify our model. We have performed a study of numerical error on the "swimming pool" example with flat seabed, starting from the initial condition $u_0(r) = 2\exp(-r^2)$, where r is the distance from the central point. We assume zero Neumann boundary conditions to obtain the wave reflection effect from the boundary of the swimming pool. We have checked the order of the time integration scheme in Fig. 14 and the spatial convergence of the method in L^2 and H_0^1 norms in Fig. 15. We have computed the relative error with respect to high fidelity solution.

6. Conclusions

We have shown that shape grammar can be applied to the generation of the computational mesh in the spherical coordinate system to model the topography and bathymetry of the entire Earth. The proposed shape grammar involves only two rules that can be applied recursively to approximate the Earth data from the Global Multi-Resolution Topography dataset until the required accuracy is reached. We have enriched the model with a finite element solver of the non-linear wave equation formulated in a spherical coordinate system and solved it using the generalized-α time integration scheme. Our numerical examples involve the tsunami caused by an asteroid in the North Atlantic Ocean, tsunami caused by the Canary Islands volcano collapse, and a tsunami caused by the earthquake in the Valparaiso region of Chile.

CRediT authorship contribution statement

Paweł Maczuga: Visualization, Validation, Software, Methodology, Investigation, Funding acquisition, Formal analysis, Data curation, Conceptualization. **Marcin Łoś:** Writing – review & editing, Writing – original draft, Visualization, Validation, Software, Methodology, Investigation, Formal analysis, Conceptualization. **Albert Oliver-Serra:** Visualization, Validation, Supervision, Software, Methodology, Investigation, Formal analysis, Conceptualization. **Eirik Valseth:** Writing – review & editing, Writing – original draft, Validation, Supervision, Methodology, Investigation, Formal analysis, Conceptualization. **Anna Paszyńska:** Writing – original draft, Visualization, Validation, Methodology, Investigation, Formal analysis, Conceptualization. **Maciej Paszyński:** Writing – review & editing, Writing – original draft, Supervision, Methodology, Investigation, Formal analysis, Conceptualization.

Declaration of competing interest

The authors declare that they have no known competing financial interests or personal relationships that could have appeared to influence the work reported in this paper.

Acknowledgments

The authors are grateful for the support from the funds that the Polish Ministry of Science and Higher Education assigned to AGH University of Krakow. The work is supported by the "Excellence initiative - research university" for AGH University of Krakow.

Data availability

Data will be made available on request.

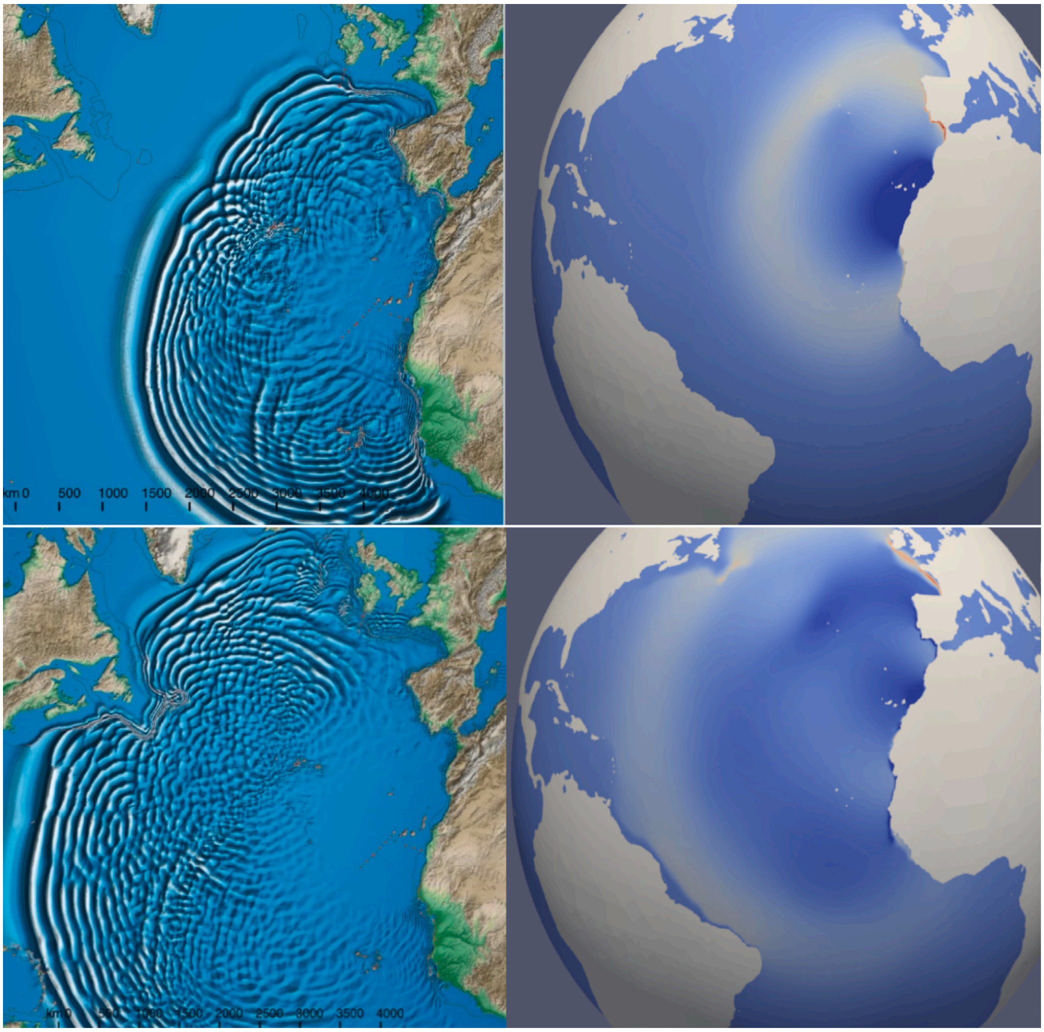

Fig. 12. Continuation of the comparison of our tsunami simulations with a simulation of a massive tsunami caused by a volcanic landslide on the island of La Palma in the Canary Islands from Steven Ward repository https://ward.sites.ucsc.edu/LaPalma-TransAtlantic-nn/. Time moment t=4h (first row), t=6h (second row).

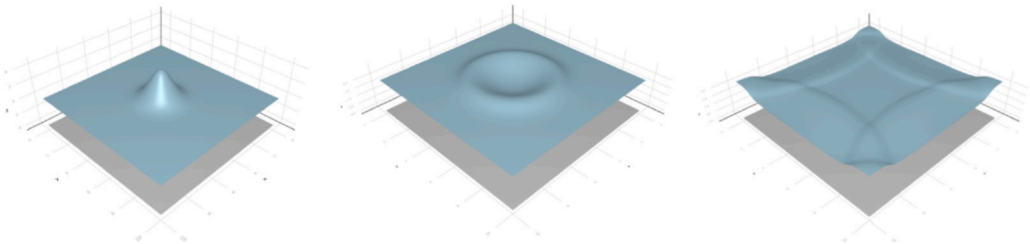

Fig. 13. Swimming pool simulation. The mesh dimensions of 256 × 256 triangular finite elements, time step $dt = 2^{-5}$.

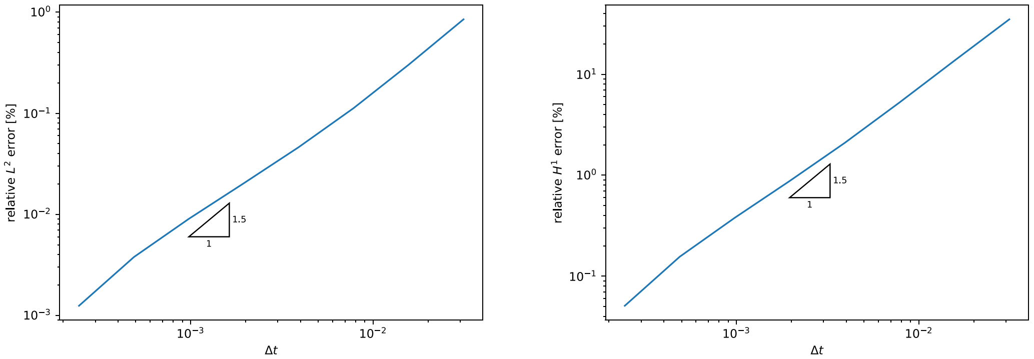

Fig. 14. How changing the mesh size (number of spatial finite elements) influence the relative error of the final solution $u(x, t = 1)$. It corresponds to the mesh dimensions from 8×8 to 1024×1024 triangular finite elements.

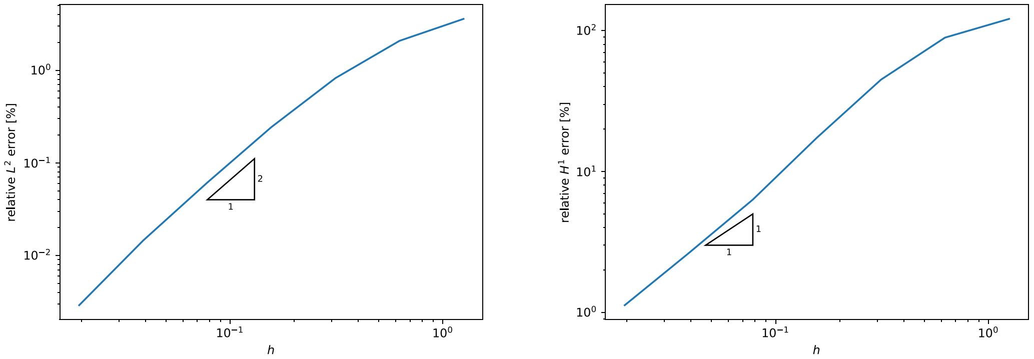

Fig. 15. How changing the time step size from $dt = 2^{-5}$ down to $dt = 2^{-13}$ influence the relative error of the final solution $u(x, t = 1)$. It corresponds to the mesh dimensions of 256×256 triangular elements. The time step was set to $dt = 2^{-13}$.

References

[1] Paweł Maczuga, Albert Oliver-Serra, Anna Paszyńska, Eirik Valseth, Maciej Paszyński, Graph-grammar based algorithm for asteroid tsunami simulations, J. Comput. Sci. 64 (2022) 101856.

[2] Paweł Maczuga, Marcin Łoś, Eirik Valseth, Albert Oliver-Serra, Leszek Siwik, Elisabede Alberdi Celaya, Anna Paszyńska, Maciej Paszyński, Simulating the aftermath of Northern European Enclosure Dam (NEED) break and flooding of European coast, Eng. Comput. (2024).

[3] Igor Kossaczký, A recursive approach to local mesh refinement in two and three dimensions, J. Comput. Appl. Math. 55 (3) (1994) 275–288.

[4] Global multi-resolution topography data synthesis, 2024, https://www.gmrt.org/. (Accessed 25 March 2024).

[5] George Stiny, James Gips, Shape grammars and the generative specification of painting and sculpture, in: IFIP Congress, 1971.

[6] Anna Paszyńska, Maciej Paszyński, Ewa Grabska, Graph transformations for modeling hp-adaptive finite element method with triangular elements, in: Proceedings of the 8th International Conference on Computational Science, Part III, ICCS '08, Springer-Verlag, Berlin, Heidelberg, 2008, pp. 604–613.

[7] Maciej Paszyński, Anna Paszyńska, Graph transformations for modeling parallel hp-adaptive finite element method, in: Roman Wyrzykowski, Jack Dongarra, Konrad Karczewski, Jerzy Wasniewski (Eds.), Parallel Processing and Applied Mathematics, Springer Berlin Heidelberg, Berlin, Heidelberg, 2008, pp. 1313–1322.

[8] Maciej Paszyński, On the parallelization of self-adaptive hp-finite element methods part I. Composite programmable graph grammar model, Fund. Inform. 93 (4) (2009) 411–434.

[9] Maciej Paszyński, On the parallelization of self-adaptive hp-finite element methods part II. Partitioning communication agglomeration mapping (PCAM) analysis, Fund. Inform. 93 (4) (2009) 435–457.

[10] Leszek Demkowicz, Computing with hp Adaptive Finite Element Method. Part I. One and Two-Dimensional Elliptic and Maxwell Problems, Taylor & Francis, CRC Press, 2006.

[11] Leszek Demkowicz, Jason Kurtz, David Pardo, Maciej Paszyński, Waldemar Rachowicz, Adam Zdunek, Computing with hp Adaptive Finite Element Method. Part II. Three-Dimensional Elliptic and Maxwell Problems with Applications, Taylor & Francis, CRC Press, 2007.

[12] Maria-Cecilia Rivara, Mesh refinement processes based on the generalized bisection of simplices, SIAM J. Numer. Anal. 21 (3) (1984) 604–613.

[13] Maria-Cecilia Rivara, Algorithms for refining triangular grids suitable for adaptive and multigrid techniques, Internat. J. Numer. Methods Engrg. 20 (4) (1984) 745–756.

[14] Krzysztof Podsiadło, Albert Oliver Serra, Anna Paszyńska, Rafael Montenegro, Ian Henriksen, Maciej Paszyński, Keshav Pingali, Parallel graph-grammar-based algorithm for the longest-edge refinement of triangular meshes and the pollution simulations in Lesser Poland area, Eng. Comput. (2021) 1–24.

[15] Efim Pelinovsky, Hydrodynamics of tsunami waves, in: Waves in Geophysical Fluids: Tsunamis, Rogue Waves, Internal Waves and Internal Tides, Springer, 2006, pp. 1–48.

[16] Wei-Yan Tan, Shallow Water Hydrodynamics: Mathematical Theory and Numerical Solution for a Two-Dimensional System of Shallow-Water Equations, vol. 55, Elsevier, 1992.

[17] George F. Carrier, Harry Yeh, Tsunami propagation from a finite source, Comput. Model. Eng. Sci. 10 (2) (2005) 113.

[18] Utku Kânoğlu, Costas Emmanuel Synolakis, Long wave runup on piecewise linear topographies, J. Fluid Mech. 374 (1998) 1–28.

[19] Ronald B. Guenther, John A. Crow, Damping of shallow water waves, in: K.-H. Hoffmann, J. Sprekels (Eds.), Free Boundary Value Problems: Proceedings of a Conference, Held at the Mathematisches Forschungsinstitut, Oberwolfach, July 9–15, 1989, Birkhäuser Basel, Basel, 1990, pp. 59–65.

[20] James T. Kirby, Fengyan Shi, Babak Tehranirad, Jeffrey C. Harris, Stephan T. Grilli, Dispersive tsunami waves in the ocean: Model equations and sensitivity to dispersion and Coriolis effects, Ocean. Model. 62 (2013) 39–55.

[21] Adrian E. Gill, William Donn, Atmosphere—Ocean Dynamics, University of Cambridge, 1982, pp. 1–662.

[22] Jintai Chung, G.M. Hulbert, A time integration algorithm for structural dynamics with improved numerical dissipation: the generalized-α method, J. Appl. Mech. 60 (2) (1993) 371–375.